



Seismically Resilient Hybrid Precast Concrete Piers with Ultrahigh-Performance Concrete

Cancan Yang, A.M.ASCE¹ and Pinar Okumus²

Abstract: This paper investigated a novel hybrid precast pier system that utilized ultrahigh-performance concrete (UHPC). The pier combines features of emulative and nonemulative (of cast-in-place construction) systems to balance self-centering and energy dissipation under seismic loading and uses UHPC to maintain that balance with low damage. An analytical model was used to study piers with varying UHPC mixes, properties of which were determined through material testing. Two large-scale pier specimens with UHPC and with varying confinement reinforcement grades were tested under quasi-static cyclic lateral loading. The test results demonstrated that the selected UHPC mix enabled the balance between bending and rocking. The rocking-induced cracking was not prevented by UHPC but was alleviated with a steel case. When the rocking-induced damage was prevented, more than 40% of the total displacement was caused by rocking at smaller drift ratios ($<0.5\%$), enabling self-centering. At larger drift ratios ($>4.5\%$), approximately 80% of the displacement was from bending, enabling energy dissipation. Replacing normal-strength steel with high-strength steel confinement did not improve the flexural capacity or ductility of UHPC. **DOI:** [10.1061/\(ASCE\)BE.1943-5592.0001713](https://doi.org/10.1061/(ASCE)BE.1943-5592.0001713). © 2021 American Society of Civil Engineers.

Author keywords: UHPC; Cyclic testing; Self-centering; Recentering; Prefabricated; Columns; Large-scale testing; Analytical model; Seismic damage mitigation; Confinement; High-strength steel; Earthquake.

Introduction

Accelerated bridge construction (ABC) can reduce the indirect cost of bridge construction and lessen the impacts of construction on traffic and roadside safety. Precast concrete bridge elements and systems have been recognized as enablers of ABC (FHWA 2018). However, precast elements have been limited to low-seismicity areas for bridge substructures. The existing precast concrete piers are classified into two categories in terms of their force transfer mechanism: (1) Emulative precast concrete pier systems refer to the systems that are emulative of cast-in-place concrete construction. They achieve monolithic concrete behavior by using special connections between column and foundation or column and cap beam (Mashal et al. 2016). (2) Nonemulative precast concrete pier systems are systems that are not expected to behave like cast-in-place concrete. By utilizing unbounded post-tensioning, nonemulative systems can develop nonlinear elasticity through joint opening and achieve self-centering (Yang and Okumus 2017a). Currently, a majority of precast concrete piers used in seismic applications are emulative systems.

Emulative connections utilize grouted sleeves (Al-Jelawy et al. 2018), bar couplers (Ameli and Pantelides 2017; Haber et al. 2014), member sockets (Haraldsson et al. 2013; Mashal and Palermo 2019a; Mohebbi et al. 2018a; Yang 2019), grout-filled ducts

(Steuck et al. 2009), and steel pipe connection (Marshall et al. 2020). Recently, a variety of damage mitigation techniques were developed for these emulative joints. These techniques and their implications on behavior are summarized in Table 1. These techniques include (1) using advanced cementitious or other materials such as ultrahigh-performance concrete (UHPC) (Mohebbi et al. 2018b; Tazarv and Saiid Saiidi 2016; Wang et al. 2018, 2019), engineered cementitious composite (ECC) (Mohebbi et al. 2018a; Tazarv and Saiid Saiidi 2016; Xu et al. 2019), ductile fiber-reinforced cementitious composite (DFRCC) (Billington and Yoon 2004), and built-in elastomeric pads (Jia et al. 2020) to prevent connection failure or flexure-induced damage in the plastic hinge zone; (2) using advanced reinforcement materials—basalt fiber-reinforced polymer (basalt FRP) bars (Cai et al. 2019), nickel–titanium shape memory alloy (Ni–Ti SMA) bars (Tazarv and Saiid Saiidi 2016) to reduce residual displacements; and (3) shifting the plastic hinge above the connection to minimize footing damage (Al-Jelawy et al. 2018; Haber et al. 2017).

Seismic damage in the nonemulative systems primarily occurs near the rocking plane and in the form of concentrated concrete spalling. Table 1 also summarizes damage mitigation techniques applicable to nonemulative systems and their impact on behavior. Adding internal energy dissipation (ED) bars to nonemulative systems has been recognized as an effective method to dissipate energy (Ou et al. 2010; Basereh et al. 2020). As such, previously studied nonemulative systems can be classified into two types, i.e., with ED bars and without ED bars. For nonemulative systems with ED bars, polyurethane (PU) damage-resistant segments at column ends and use of high-strength ED bars were shown to minimize rocking-induced damage and enhance self-centering, respectively (Nikoukalam and Sideris 2017; Tong et al. 2019). Nonemulative systems with ED bars are named hybrid systems by some researchers in the literature. For nonemulative systems without ED bars, seismic damage was shown to be controlled by the following means: (1) using UHPC or glass-FRP-encased concrete in the segment above the foundation to minimize rocking-induced damage (Guo et al. 2016; Yang and Okumus

¹Assistant Professor, Dept. of Civil Engineering, McMaster Univ., Room 339, John Hodgins Engineering, 1280 Main St. West, Hamilton, ON, Canada L8S 4L7 (corresponding author). ORCID: <https://orcid.org/0000-0001-8596-2265>. Email: yangc106@mcmaster.ca

²Associate Professor, Dept. of Civil, Structural and Environmental Engineering, Univ. at Buffalo, The State Univ. of New York, 222 Ketter Hall, Buffalo, NY 14260. ORCID: <https://orcid.org/0000-0002-2197-3261>. Email: pinaroku@buffalo.edu

Note. This manuscript was submitted on July 25, 2020; approved on January 6, 2021; published online on March 25, 2021. Discussion period open until August 25, 2021; separate discussions must be submitted for individual papers. This paper is part of the *Journal of Bridge Engineering*, © ASCE, ISSN 1084-0702.

Table 1. Summary of the literature on the damage mitigation techniques for emulative and nonemulative precast concrete pier systems

System	Reference	Joint	Damage mitigation technique	Major conclusion
Emulative	Al-Jelawy et al. (2018) and Haber et al. (2017)	Grouted sleeve	Shift the plastic hinge above the grouted sleeve region	• Plastic hinging can be developed above the sleeve region to minimize damage to footing
	Wang et al. (2019)		Adopt lap-spliced bars and UHPC grout	• The system can emulate the behavior of cast-in-place systems
	Xu et al. (2019)	Member socket	Replace concrete with ECC at the grouted sleeve connection zone	• ECC can effectively alleviate flexure-induced damage to the system
	Billington and Yoon (2004)		Use DFRCC in the potential plastic hinging region	• DFRCC can add hysteretic energy dissipation to the system and provide damage tolerance.
	Mohebbi et al. (2018a, b)	Grout-filled duct	Use UHPC and ECC in the plastic hinge zone	• UHPC and ECC reduced column plastic hinge damage
	Jia et al. (2020)		Incorporate a novel built-in elastomeric pad into the plastic hinge zone	• The built-in elastomeric pad minimized local concrete damage at the bottom of columns and increased energy dissipation
	Cai et al. (2019)	Bar coupler	Use basalt FRP longitudinal reinforcement	• Basalt FRP can reduce seismic damage and improve self-centering energy dissipation and ductility
	Tazarv and Saiid Saiidi (2016)		Adopt UHPC-filled duct connection and use reinforcing NiTi SMA bars and ECC shell in the plastic hinge zone	• UHPC-filled duct connection had no damage. Precast systems had significantly lower damage than the reference cast-in-place column
Nonemulative	Wang et al. (2018)		Use four UHPC plates, tied by replaceable dissipators, to surround core concrete	• Damage was concentrated in UHPC plates and replaceable dissipators. Damage to core concrete was minimal
	Nikoukalam and Sideris (2017)	With ED bars	Use PU damage-resistant segments at the column ends	• PU can allow the system to accommodate large rotations without evident damage
	Tong et al. (2019)		Use high-strength ED bars	• The benefits of high-strength ED bars include the enhanced load-carrying capacity, energy dissipation, and self-centering
	Sideris et al. (2014) and Yang et al. (2019)	Without ED bars	Apply silicone at the segmental interface	• By initiating sliding between precast segments, rocking-induced damage can be reduced and bending is eliminated
	Guo et al. (2016)		Incorporate basalt FRP tendons and external energy dissipators and use glass FRP jacket to encase the bottom of the pier	• The system exhibited desirable self-centering and energy dissipation
	Mashal and Palermo (2019b)		Use DCRs that incorporate externally attached metallic dissipaters	• Test results show that using DCR can effectively eliminate damage and residual drift ratio at larger drift ratios
	Liu (2018)		Use multiple sets of dissipative devices across one rocking interface and have multiple rocking interfaces along the pier's height	• The redundancy and robustness of the pier can be improved by activating the dissipative devices and rocking in a staged manner
	Yang and Okumus (2017b)		Use UHPC in the column segment above the foundation	• UHPC led to minimal compression damage at displacements much larger than the seismic demand. The difference in damage of UHPC segments with and without mild steel was negligible
	Fang et al. (2020)		Use extended pier base and SMA washer springs	• SMA washer springs can provide stable flag-shaped hysteresis with negligible residual deformation and moderate energy dissipation

Note: DCR = dissipative controlled rocking connection.

2017b); (2) using Basalt FRP tendons or SMA washer springs to improve self-centering (Guo et al. 2016; Fang et al. 2020); (3) incorporating externally attached metallic dissipaters (Mashal and Palermo 2019b); and (4) applying low-friction coefficient materials (silicone) at precast segment interfaces to introduce sliding (Sideris et al. 2014; Yang et al. 2019).

The damage mitigation techniques presented in Table 1 have been experimentally and analytically demonstrated to be effective. These techniques rely on the enhanced mechanical properties of advanced materials or supplemental energy dissipation devices to address the limitations specific to existing precast concrete systems (i.e., emulative or nonemulative systems). The novelty of the

damage mitigation solution proposed in this paper is the combination of a new hybrid precast pier system and UHPC. The new hybrid precast pier system takes advantage of emulative and nonemulative systems for balancing self-centering and energy dissipation, in addition to using UHPC to maintain that balance by minimizing damage.

Research Scope and Significance

The large-scale quasi-static cyclic test results show that the hybrid pier with normal concrete (NC) can develop both bending and

rocking, thereby striking a balance between self-centering and energy dissipation. However, damages occurred to the hybrid pier include concrete cracking and spalling near the rocking plane and within the emulative joint. Controlling these damages is important for hybrid piers because the damage near the rocking plane affected the expected balance between rocking and bending response and damage within the emulative joint due to the prying action caused strength degradation. As such, this research aims to incorporate UHPC—a fiber-reinforced cementitious material with high compressive strength and sustained postcracking tensile strength—into the hybrid pier to mitigate the aforementioned damages observed in hybrid precast piers under lateral loading. To this end, this research will proceed through three phases with the following objectives: (1) characterize UHPC properties through material-scale tests; (2) conduct a parametric study of hybrid piers with varying UHPC mixes in the bending segment; and (3) perform large-scale quasi-static testing of two hybrid piers with UHPC and varying confinement reinforcement grades. The paper presents unique test data and conclusions on the seismic performance of precast concrete hybrid piers, the behavior of UHPC under bending in hybrid piers, and the behavior of UHPC with various confinement amounts. These outcomes can assist practitioners in developing appropriate UHPC-based solutions for mitigating seismic damages for hybrid precast piers.

Hybrid Precast Pier Concept and Need for UHPC

Concept and Design Methods of the Hybrid Precast Pier

The hybrid precast pier was developed to combine the advantages of emulative and nonemulative systems. It is composed of multiple precast column segments. For the piers investigated in this paper, three column segments are used, as shown in Fig. 1. The bottom column segment is designed to have an emulative connection to the foundation. The middle and upper column segments have nonemulative connections to the adjacent members so that they can rock over the bottom column segment. The columns can be constructed with a precast foundation and a precast pier cap for rapid construction. For the pier presented in this paper, the bottom segment is connected to the foundation by a socket type, i.e., emulative joint. The upper two column segments and cap beam are connected to the adjacent precast elements with unbonded post-tensioning strands, i.e., nonemulative joints, without any continuous mild reinforcement between segments. Unbonded post-tensioning runs across all column segments, cap beam, and foundation.

Under lateral load, the bottom segment is expected to bend like a monolithic column and is therefore referred to as the *bending segment* (Fig. 1). The plastic hinge forming at the emulative joint can provide energy dissipation to the pier. The upper column segments are expected to rock over the bottom segment and therefore referred to as the *rocking segment* (Fig. 1). Rocking can enable self-centering after the removal of lateral load. The hybrid pier has the potential to balance energy dissipation and self-centering as it combines bending and rocking column segments.

The design philosophy is to develop balanced bending and rocking response based on the ground motion intensity (maximum displacement demand). For a small displacement demand, rocking is expected to make up a relatively large percentage (>40%) of the total displacement, enabling self-centering. Rocking response can reduce the demand for bending, postponing concrete cracking and rebar yielding at the emulative joint. For a larger displacement demand, bending is expected to dominate the overall response by

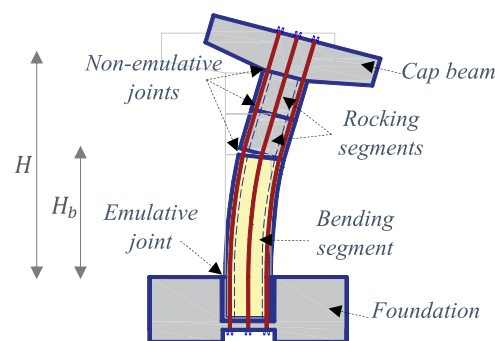


Fig. 1. Hybrid pier system with nonemulative and emulative joints.

contributing to more than 80% of the total displacement, thereby enabling the development of sufficient energy dissipation.

A mechanics-based analytical model was used to quantitatively evaluate the hierarchical activation of bending and rocking response. The analytical model can predict the load–displacement response and bending/rocking contributions to the total displacement of the pier under lateral load. The rocking and bending responses were related to global responses based on the proportionality of the moments at bending and rocking bases. Taking into account the coupled impact of bending and rocking on post-tension, a series of iterative calculations were performed to achieve section equilibrium at both bending and rocking bases. The details of the analytical model are in Yang (2019).

UHPC

The hybrid precast pier is composed of multiple precast column segments. For the piers investigated in this paper, three column segments are used, as shown in Fig. 1. The bottom column segment is designed to have an emulative connection to the foundation. The middle and upper column segments have nonemulative connections to the adjacent members so that they can rock over the bottom column segment. The columns can be constructed with a precast foundation and a precast pier cap for rapid construction. For the pier presented in this paper, the bottom segment is connected to the foundation by a socket type, i.e., emulative joint. The upper two column segments and cap beam are connected to the adjacent precast elements with unbonded post-tensioning strands, i.e., nonemulative joint, without any continuous mild reinforcement between segments. Unbonded post-tensioning runs across all column segments, cap beam, and foundation.

Under lateral load, the bottom segment is expected to bend like a monolithic column and is therefore referred to as the *bending segment* (Fig. 1). The plastic hinge formed at the emulative joint can provide energy dissipation to the pier. The upper column segments are expected to rock over the bottom segment and therefore referred to as the *rocking segment* (Fig. 1). Rocking can enable self-centering after the removal of lateral load. The hybrid pier has the potential to balance energy dissipation and self-centering as it combines bending and rocking column segments.

A previous study on hybrid piers with normal concrete (Yang 2019) showed that concrete near the rocking joints is vulnerable to cracking and crushing, shifting the balance of rocking and bending toward rocking. In addition, prying of the column within the socket-type connection was observed to reduce lateral strength. UHPC was utilized in the bending column segment of the hybrid pier to alleviate rocking-induced damage and prying within the socket connection to the foundation. ACI 318-19 (ACI 2019) and AASHTO (2017) require higher-confinement reinforcement amounts for UHPC than it does for normal concrete, as

confinement need is a function of the compressive strength. Therefore, UHPC was utilized in the bending column segment of the hybrid pier with various amounts of confinement reinforcement to understand the impact of confinement on the bending behavior of UHPC and on the hybrid pier.

Selection of a UHPC Mix for the Bending Segment

UHPC was used in the bending column segment of the hybrid pier for improved seismic performance (reduced spalling, well-distributed narrow cracking, and enhanced resistance against prying action within the foundation). A UHPC mix was selected so that the replacement of NC by UHPC improves damage control without compromising the balance between bending and rocking. Material testing was performed on various mixes of UHPC. All UHPC mixes were commercially available mixes called Ductal (LafargeHolcim 2009). Although a commercial mix was used in this research, the results are applicable to any UHPC mixes with comparable compressive and tensile strengths and toughnesses. Compression and tension constitutive properties were obtained, and crack characteristics were documented based on the material test results. Compressive and tensile toughnesses were used to quantify UHPC's ability to sustain strength after cracking and spalling. A parametric study was completed to understand the impact of different UHPC mixes on the behavior of hybrid piers under lateral load.

Material Tests

UHPC Mixes

Five UHPC mixes were investigated. These mixes utilized two pre-mix types (AN1000 and JS1000), two fiber types [PVA (polyvinyl alcohol) and steel] and three fiber volume ratios (1%–4%), as summarized in Table 2. Both steel and PVA fibers were 0.008 in. (0.2 mm) in diameter and 0.5 in. (12.7 mm) in length. The design strengths of AN1000 and JS1000 are 120 MPa (17 ksi) and 150 MPa (20 ksi), respectively. All mixes were air-cured for at least 28 days. The curing method was kept consistent between UHPC material tests and large-scale UHPC hybrid pier tests.

Table 2. Ductal UHPC mixes

Mix no.	Mix design	Fiber type and amount
1	AN1000	2% PVA fiber
2	JS1000	4% PVA fiber
3		2% Steel fiber
4		2% PVA fiber
5		1% Steel fiber

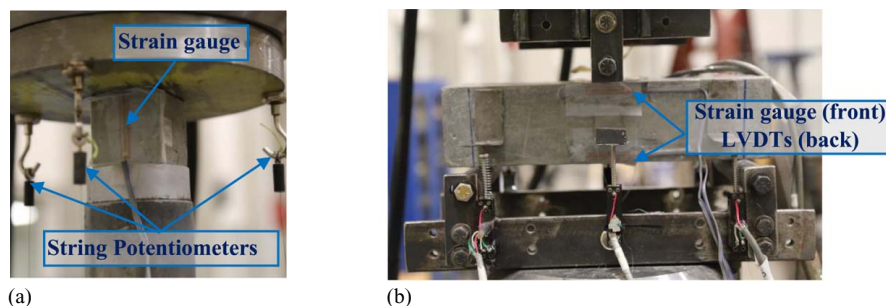


Fig. 2. Test setup and instrumentation for (a) compression tests; and (b) flexure tests.

Material Test Setup

UHPC specimens were tested under compression and flexure through an MTS Axial-Torsion Universal testing machine at the University at Buffalo, the State University of New York. For both compression and flexure tests, two specimens were tested for each mix. Compression specimens were 50.8 mm by 50.8 mm (2 in. by 2 in.) cubes according to ASTM C109/C109M (ASTM 2016). The compression test setup and instrumentation are shown in Fig. 2(a). Strain gauge and string potentiometers measured the compressive strain in the linear and nonlinear ranges, respectively. Three-point flexure tests were performed to obtain the flexural capacity of the prisms, as shown in Fig. 2(b). Flexure specimens were 76.2 mm by 76.2 mm by 304.8 mm (3 in. by 3 in. by 12 in.) prisms. The prisms were supported by two rollers spaced at 254 mm according to ASTM C1609/C1609M (ASTM 2019b) and ASTM C1856/C1856M (ASTM 2017). Strains measured by the strain gauges and linear variable displacement transducers (LVDTs) were used to calculate curvature in the linear and nonlinear ranges, respectively.

Material Test Results

Fig. 3 shows the measured stress–strain relationships of all UHPC mixes. Each graph shows the stress–strain relationships obtained from two specimens of the same mix. All UHPC mixes exhibited considerably higher compressive strengths compared to conventional concrete. The average compression strengths were 148.5 MPa (21.5 ksi), 126.3 MPa (18.3 ksi), 151.8 MPa (22 ksi), 119.9 MPa (17.4 ksi), and 146.6 MPa (21.3 ksi) for Mix-1, Mix-2, Mix-3, Mix-4, and Mix-5, respectively. For all mixes, gradual softening was observed after peak strength in compression. Fig. 4 shows the moment–curvature relationships obtained from the flexure tests of all mixes. Curves represent the results from the two specimens of the same mix. The curvature was calculated as the ratio of the difference of the strains measured at the extreme compression and tension layers over the cross-sectional depth. Unlike what is expected of conventional concrete, UHPC prisms maintained their integrity after cracking and achieved a larger curvature ductility due to fiber bridging.

Constitutive Models for the UHPC Mixes

Compression

The compressive stress–strain relationships of mixes were approximated as piecewise linear functions. The elastic range of stress–strain relationship was determined to be linear up to 90% the peak stress, and the elastic modulus was calculated according to Graybeal (2006). The nonlinear compressive stress–strain relationship was assumed to be trilinear. The four points that define the stress–strain relationship are shown in Fig. 3 (points A, B, C, and D). By integrating the developed compressive stress–strain

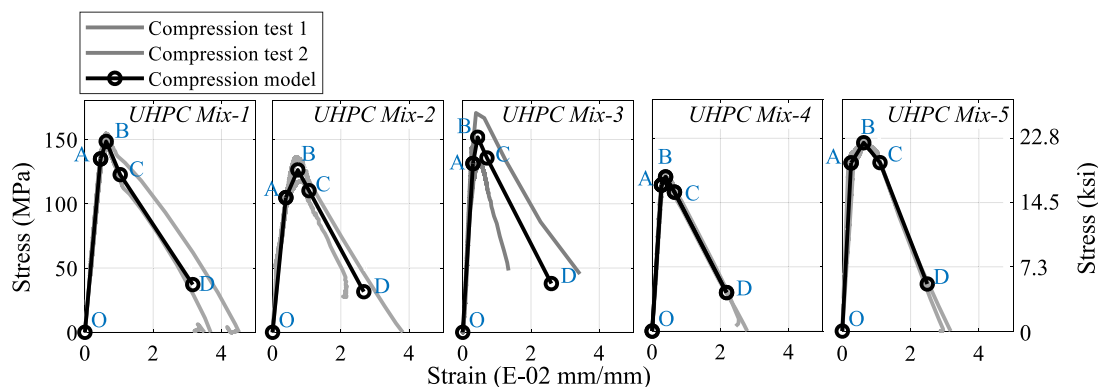


Fig. 3. Measured compressive stress–strain relationship and compressive constitutive models of UHPC mixes.

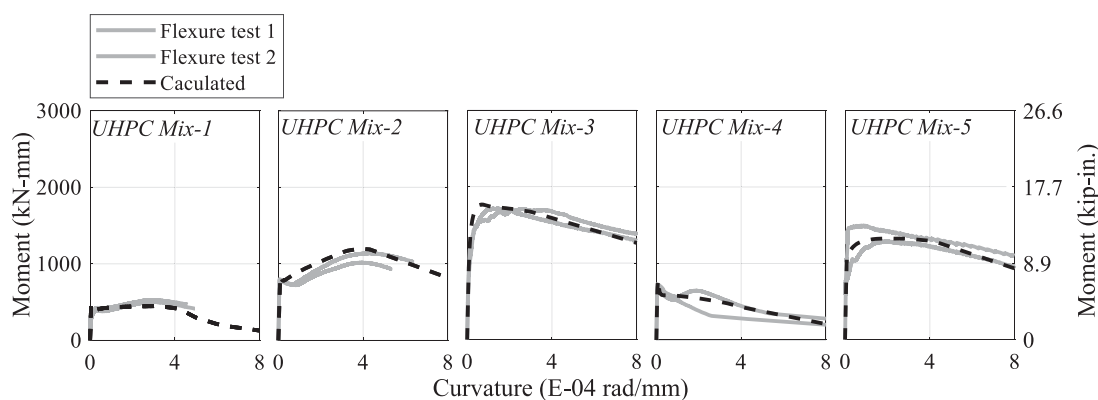


Fig. 4. Measured and calculated moment–curvature relationships for UHPC mixes.

relationships, the compressive toughness values were calculated to be 3.29, 2.43, 2.64, 1.80, and 2.68 $\text{N} \cdot \text{mm}^{-2}$ for Mix-1, Mix-2, Mix-3, Mix-4, and Mix-5, respectively.

Tension

Tensile stress–strain relationship of UHPC can be obtained by direct tension tests or modulus of rupture tests. Considering the sensitivity of the direct tensile test results to the test setup (Baby and Graybeal 2012), the tensile stress–strain relationships for UHPC were derived based on the measured moment–curvature responses in flexure tests. Note that the tensile strength and ductility from flexure tests tend to be slightly higher than that from direct tensile tests due to strain gradient effects (Baby et al. 2013). For all UHPC mixes, the tensile stress–strain relationship is assumed linear when the stress was below the tensile strength. The tensile stress–strain relationship for each UHPC mix was determined by defining four points shown in Fig. 5 (points A, B, C, and D). Fig. 4 shows the measured moment–curvature responses for all UHPC prisms as compared to the ones predicted using the tensile stress–strain relationship shown in Fig. 5. By integrating the derived tensile stress–strain relationships, the tensile toughness values were calculated to be 6.02×10^{-2} , 1.62×10^{-1} , 2.44×10^{-1} , 6.50×10^{-2} , and $1.88 \times 10^{-1} \text{ N} \cdot \text{mm}^{-2}$ for Mix-1, Mix-2, Mix-3, Mix-4, and Mix-5, respectively.

Hybrid Precast Piers with UHPC

UHPC with exceptional mechanical properties offer great potential to effectively control damages in hybrid precast piers. In contrast, due to the high tensile strength, stiffness, and ductility of UHPC,

UHPC in the bending segment of hybrid precast piers can lead to a higher flexural stiffness and moment capacity at the emulative joint. If rocking dominates the response of the hybrid pier, the bending segment may not be able to reach its moment capacity. As such, the optimum UHPC mix for the bending segment of hybrid piers is defined based on the following two criteria: (1) achieve the expected hierarchical activation of bending and rocking response; and (2) provide adequate damage tolerance in hybrid piers. To assess the balance between rocking and bending contributions, the bending contribution ratio of hybrid piers with various UHPC mixes in the bending segment was calculated using an analytical model in section “Concept and Design Methods of Hybrid Precast Pier.” To assess the damage tolerance of UHPC, the tensile and compressive toughness of varying UHPC mixes were compared to each other.

The constitutive models for the UHPC mixes were implemented into the analytical model (Yang 2019) to calculate the response of the hybrid precast piers with UHPC. The cross section, post-tension, and reinforcement layout of the bending and rocking column segments of the hybrid pier used for this study are shown in Fig. 6 and are selected based on a hybrid pier design with normal concrete (Yang 2019). Viable ranges of the design parameters that affect the lateral load behavior were determined for normal concrete hybrid piers by Yang (2019) as follows: (1) the initial post-tension force: $PT_{ini} = 89\text{--}133 \text{ kN}$ (20–30 kips) (per strand or 10%–15% of axial compression capacity calculated using the compressive strength of NC); (2) the longitudinal reinforcement ratio of the bending segment: $\rho_{bending} = 1.3\%\text{--}1.8\%$; and (3) the ratio of the bending segment height to the total column height ($\lambda_b = H_b/H$ in Fig. 1): $\lambda_b = 50\%\text{--}60\%$. In this paper, the impact of UHPC mixes

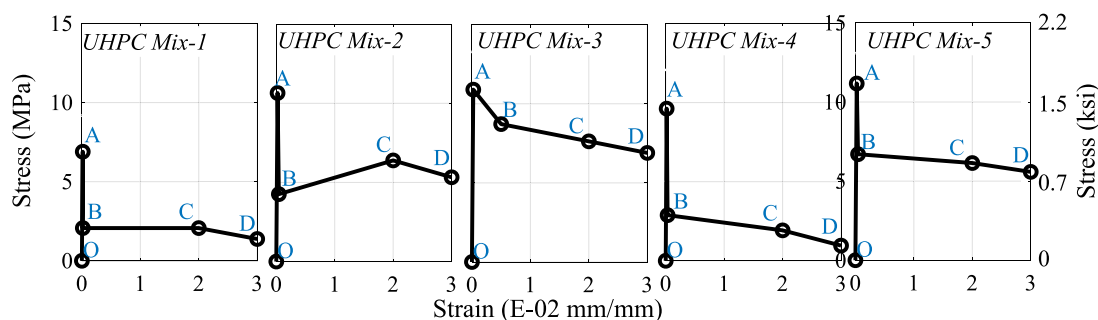


Fig. 5. Tensile constitutive models of UHPC mixes.

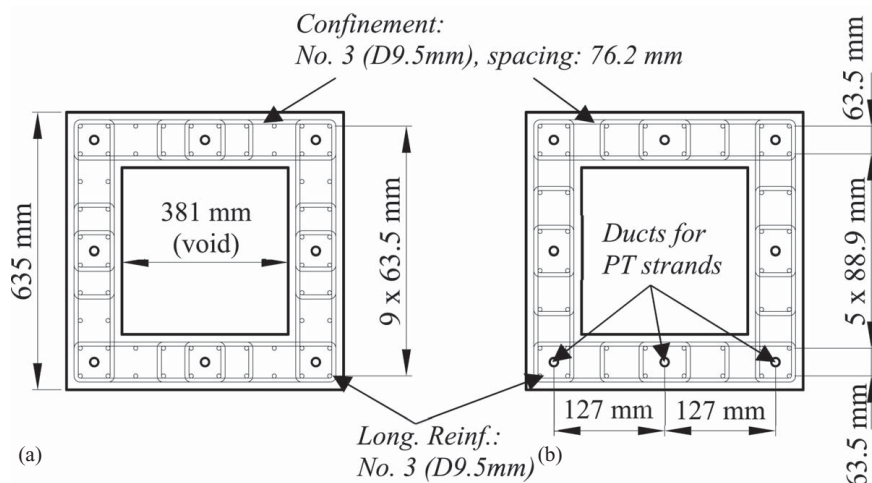


Fig. 6. Reinforcement details of the rectangular hollow sections for (a) rocking column; and (b) bending column segments (1 mm = 0.039 in.).

on the lateral load behavior is investigated for this range of initial post-tension, height ratio, 1.3% longitudinal bending reinforcement ratio, and a total height of 3,448 mm.

Fig. 7 shows the bending contribution ratio with respect to the lateral displacement at the loading point for hybrid piers with UHPC mixes 1–5 and for varying initial post-tension and height ratios. The bending contribution ratio is defined as the ratio of bending drift to total drift. Bending drift was calculated as the ratio of lateral displacement at the top of the bending segment to the bending segment height (H_b in Fig. 1). The total drift was calculated as the lateral displacement of the loading point (midheight of the pier cap) to the total height (H in Fig. 1).

To select a UHPC mix well suited for the hybrid pier, the tensile and compressive toughnesses of varying UHPC mixes were compared to each other to assess their damage tolerance, as seen in Figs. 8(a and b), respectively. The bending contribution ratio, averaged over drift ratio amplitudes of 0.4%–6%, over initial post-tension force (PT_{ini}) of 89–133 kN (20–30 kips) per strand, and over bending to total height ratio (λ_b) of 0.5–0.6, was also compared among different UHPC mixes, as shown in Fig. 8(c). The analytical model analysis results show that the bending contribution ratio is minimally impacted by the compressive toughness of UHPC. However, the bending contribution ratio decreases with an increase in UHPC's tensile toughness. Hybrid piers with UHPC Mix 3 (the largest tensile toughness of all mixes) had the lowest bending contribution ratio. From Fig. 8(c), only UHPC Mix-1 and Mix-4 were capable of maintaining the balance between bending and rocking, i.e., with an average bending contribution ratio of 50%. For the other UHPC mixes, the average bending

contribution ratios were below 30%, showing that displacement was dominated by rocking response. UHPC Mix-1 had 83% higher compressive toughness than UHPC Mix-4, showing greater ability for damage mitigation in the hybrid system. Therefore, UHPC Mix-1 with AN1000 mix design and 2% PVA fiber by volume was selected for the bending segment.

Experimental Program

Hybrid Pier Specimens

Two 1–2.4-scale hybrid precast pier specimens were designed and constructed. The design details of the hybrid pier specimens followed those of the nonemulative piers tested by Yang and Okumus (2017b) but were modified to incorporate both emulative and non-emulative joints in a single pier. A five-span single-cell box girder concrete considered by Megally et al. (2002) was adopted as the prototype bridge. An elevated view of the specimens is shown in Fig. 9(a). The segment cross section, post-tension, and mild steel reinforcement layout of rocking and bending segments are shown in Figs. 6(a and b). The bending segment was made of UHPC mix 1, whereas other column segments, cap beam, and foundation were made of normal concrete with 5-ksi (34.5 MPa) design compression strength. The dimension of the cap beam was 2,407 mm by 737 mm by 597 mm (94¼ in. by 29 in. by 23.5 in.). The longitudinal and transverse reinforcement ratios were 0.4% and 1.6%, respectively. Additional reinforcement was provided to enhance the post-tensioning anchorage region and the actuator connection

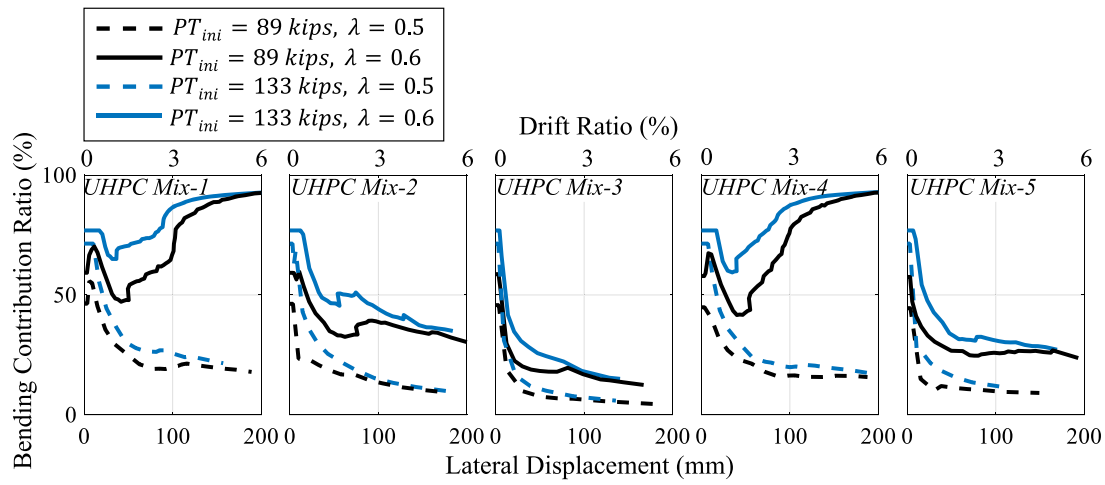


Fig. 7. Bending contribution ratio of the hybrid pier with UHPC mixes.

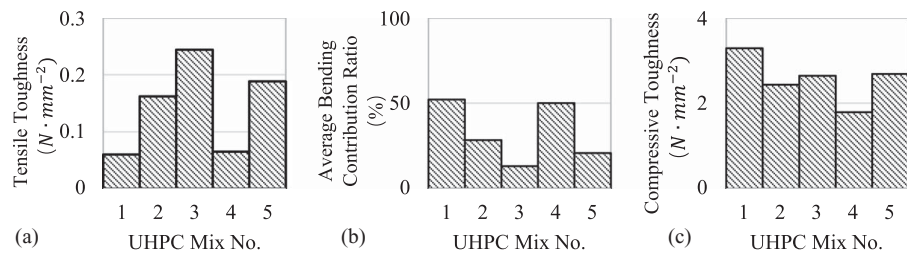


Fig. 8. Comparison of (a) tensile toughness; (b) compressive toughness; and (c) average bending contribution ratio for all UHPC mixes.

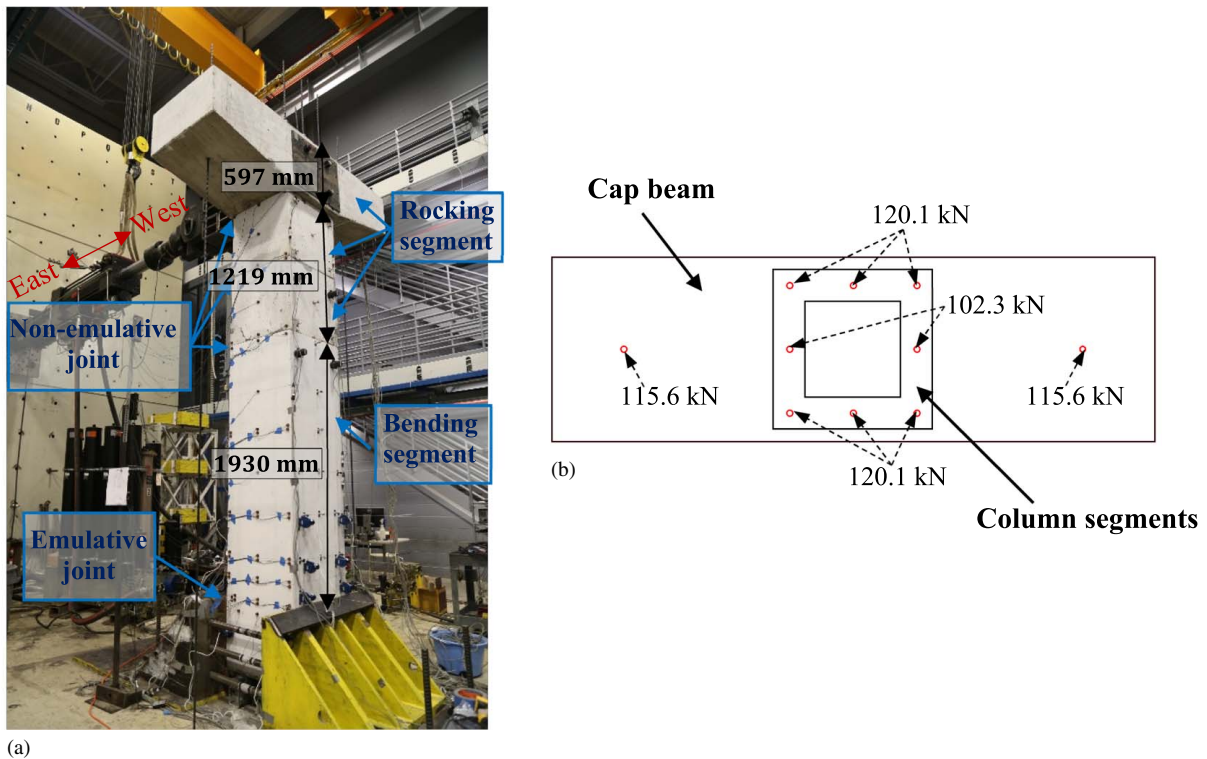


Fig. 9. (a) Specimen and test setup; and (b) initial post-tension force shown on a plan view.

region. The target initial post-tension force on each strand (PT_{ini}) is presented in Fig. 9(b). This corresponds to 13% of the axial compression capacity of the pier calculated using the compressive strength of NC. This figure also shows two post-tension strands anchored to the pier cap with 115.6 kN (26 kips) force on each strand. This corresponds to 2.6% of the axial compression capacity of the pier calculated using the compressive strength of NC. These strands were used to simulate the weight of the superstructure. The longitudinal reinforcement ratio of the bending segment ($\rho_{bending}$) was 1.32%. The longitudinal reinforcement ratio of the rocking segment was 1.8% after a nonemulative pier tested by Yang and Okumus (2017b). The height ratio (λ_b) was 54%. All longitudinal reinforcement bars were Grade 60 steel (ASTM A615/A615M, ASTM 2020). The details for the cap beam and foundation can be found in Yang (2019).

The difference between the two specimens was the grade of the confinement reinforcement steel type used in the bending column segment. The average confinement reinforcement volumetric ratio of each flange of the hollow section of the two orthogonal directions was 1.8%. [Grade 60 (ASTM A615/A615M, ASTM 2020)], and the Specimen I used normal-strength steel confinement volumetric ratios were 54% and 41% of the minimum requirement of ACI 318-19 (ACI 2019) and AASHTO (2017), respectively. Following the code requirements for confinement reinforcement may result in an impractical amount of reinforcement for UHPC, particularly for hollow sections. Therefore, Specimen II used high-strength steel [Grade 120 (ASTM A1035/A1035M, ASTM 2019a)] confinement. The confinement volumetric ratios of Specimen II were 109% and 82% of the minimum requirement of ACI 318-19 (ACI 2019) and AASHTO (2017), respectively. The average yielding strength of the Grade 60 rebar coupons was 483.3 MPa (70 ksi). Grade 120 rebar did not have an evident yielding plateau. As such, the average yield strength [962 MPa (140 ksi)] was obtained by using 0.2% strain offset rule. The average ultimate strength and fracture strain were 722.6 MPa (104.8 ksi) and 0.19 for Grade 60 rebar and were 1,224.5 MPa (177.6 ksi) and 0.15 for Grade 120 rebar, respectively.

Test Scheme

Two sets of quasi-static cyclic tests were conducted on each specimen (Fig. 10). These tests were referred to as Test Phase I and Test Phase II. Each specimen was loaded up to 3% drift ratio in Test Phase I and loaded until failure or to the maximum displacement of the loading protocol in Test Phase II. Test Phase I focused on investigating damage near the nonemulative (rocking) joint. Test Phase II focused on investigating damage occurring at the emulative (bending) joint. During Test Phase I of Specimen I, the region of the bending segment near the nonemulative joint underwent lateral dilation due to rocking-induced compression and shear friction. After Test Phase I, Specimen I was disassembled, and a steel case was added to confine the top of the bending segment to proceed to Test Phase II. The steel case was made by welding five steel plates with a thickness of 6.4 mm (1/4 in.). The steel case encased the top region of the bending segment over a height of 101.6 mm (4 in.) without being adhesively or mechanically connected to the column. Specimen II was initially built with the top of the bending segment confined by a steel case. Specimen II was initially built with the top of the bending segment being confined by a steel case. The loading protocol of the quasi-static tests included sets of symmetric cycles of increasing displacement amplitudes. Each displacement amplitude had two repeating cycles. Additional details of the loading protocol are available in Yang (2019).

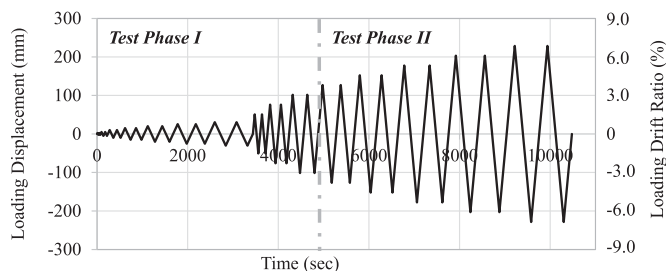


Fig. 10. Loading protocols.

Test Setup and Instrumentation

Cyclic loading was applied in the east–west direction (Fig. 9) through a 979-kN (220-kips) capacity hydraulic actuator. The bending segment was inserted into a steel bracket fixture by 520.7 mm (82% of the column cross section depth) to create a socket-type joint with rotation restraint (Fig. 1). Steel brackets were designed to remain elastic through testing. The two steel brackets were post-tensioned to each other using six horizontal threaded rods. Each threaded rod was post-tensioned to about 178 kN (40 kips) initially to create contact (friction) between the pier and brackets without damaging the pier specimen before testing. The steel brackets were vertically post-tensioned to the strong floor to prevent sliding or uplifting (Fig. 19).

Load cells were used to measure the axial force on each post-tensioning tendon. In total, 20 string potentiometers and 25 LVDTs were instrumented to capture gap opening at nonemulative joints to monitor vertical slip of the pier from the steel bracket, shear slip between pier segments, slip of the steel bracket fixture, elongation or shortening of concrete, and the displacements in the loading direction along the height of the specimen. Strain gauges were mounted on the longitudinal and transverse rebar of the bending segment next to the emulative joint. A coordinate tracking system was used to track the three-dimensional motion of LED sensors mounted on the north face of the pier specimens. The data outliers due to light variations were removed by a low-pass filter. Additional details are in Yang (2019).

Test Results

Results of Test Phase I

Damage Assessment

For both Specimens I and II, the apparent concrete damage of Test Phase I was primarily near the top of the bending segment, as seen in Fig. 11. No damage was observed in the cap beam for Specimens I and II. For Specimen I, the first rocking-induced cracking at the top of the bending segment was observed at 2.3% drift ratio and propagated downward vertically. For Specimen II, due to the confinement by the steel case, damage at the top of the bending segment was limited to hairline cracking. Spalling failure observed in a normal concrete bending segment near the rocking plane (Yang et al. 2019) was alleviated with UHPC. However, the selected UHPC mix was not able to prevent vertical crack initiating at the rocking plane.

Global Force–Displacement Response

Fig. 12 shows the lateral force versus lateral displacement hysteretic response of Test Phase I for Specimens I and II. In both specimens, force in all of the post-tension strands remained below the nominal yield force, the longitudinal reinforcement bars within

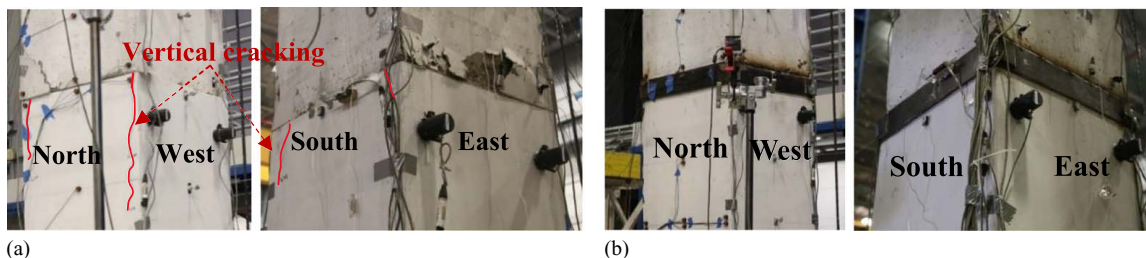


Fig. 11. Damage after Test Phase I at nonemulative joints for (a) Specimen I; and (b) Specimen II.

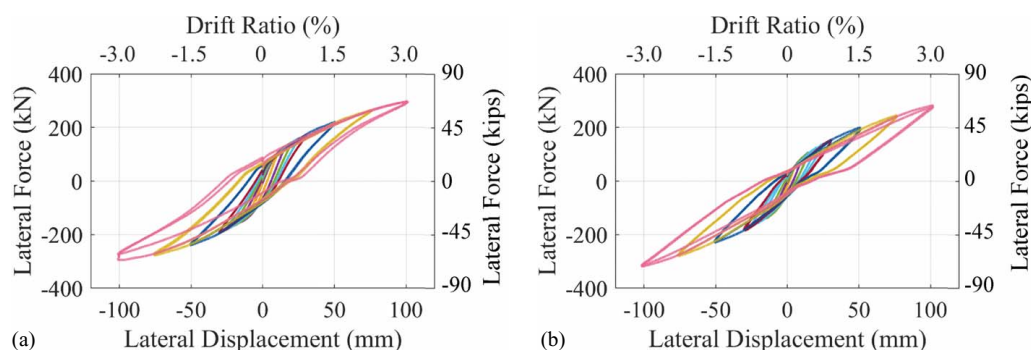


Fig. 12. Global force-displacement relationships of Test Phase I for (a) Specimen I; and (b) Specimen II.

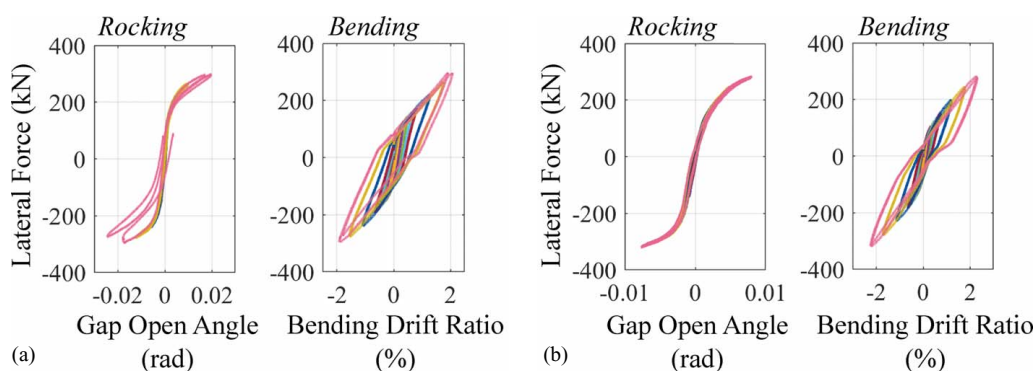


Fig. 13. Displacement decomposition of Test Phase I for (a) Specimen I; and (b) Specimen II.

the bending column segment yielded and played a role in energy dissipation. For Specimen I, the lateral strength consistently increased until the displacement reached 3% drift ratio in the negative loading direction. After this displacement, the rocking-induced vertical crack at the top of the bending segment propagated downward, reducing resistance to rocking, reducing strength, and increasing rocking displacements. Specimen II had a steel case at the top of the bending column segment. This specimen had a stable increase of lateral strength at all displacement magnitudes. The pinching effect was more evident in Specimen II than it was in Specimen I due to the prevalence of higher bending displacements over rocking displacements, as discussed in section “Displacement Source.”

Displacement Source

Fig. 13 shows the rocking and bending responses for Test Phase I. Gap opening occurred only between the bending segment and

the lower rocking segment for both specimens. Rocking response is presented as the relationship between lateral force and gap opening angle at this joint. The gap opening angle was calculated by dividing the difference between the elongation measured at the tension side and shortening measured at the compression side of the column by the column width. Bending response is presented as the relationship between lateral force and bending drift ratio. The bending drift ratio was calculated as the ratio between the lateral displacement measured at the top of the bending segment and the height of the bending column segment above the top of the steel brackets. Both specimens had negligible residual displacements due to rocking. Pinching, energy dissipation, and residual displacements were observed in the force-bending drift ratio hysteresis loops for both specimens in the bending response. For Specimen I, the reduction of the rocking stiffness, associated with the propagation of the crack from the top of the bending segment downward, is evident at the last half-cycle of the lateral force-gap opening

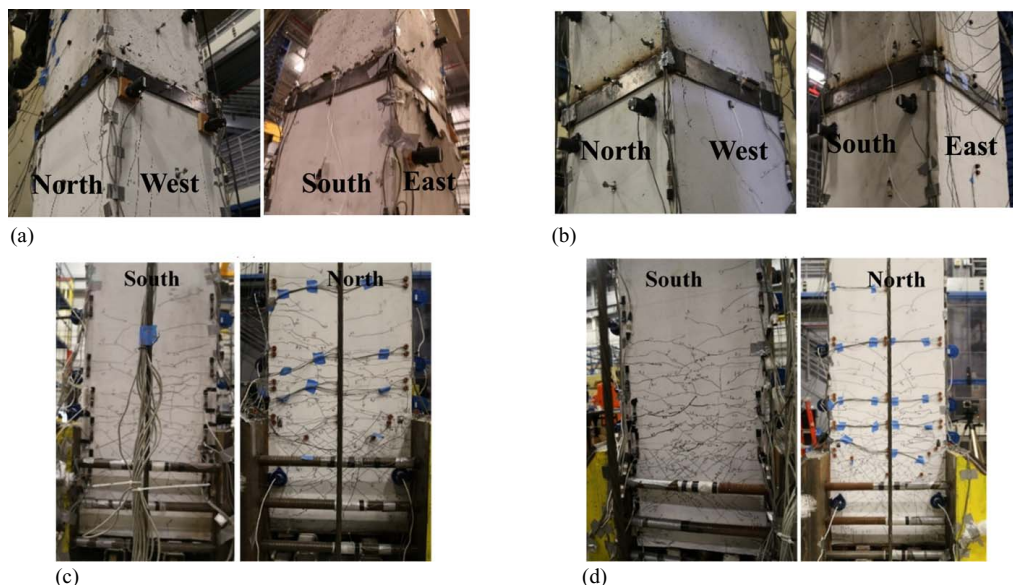


Fig. 14. Damage after Test Phase II at nonemulative joints for (a) Specimen I; and (b) Specimen II and at emulative joints for (c) Specimen I; and (d) Specimen II.

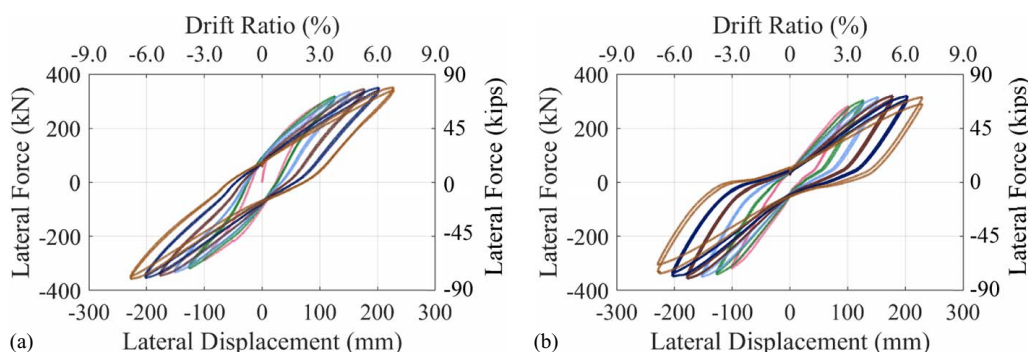


Fig. 15. Global force-displacement relationships of Test Phase II for (a) Specimen I; and (b) Specimen II.

angle plot. Specimen II demonstrated stable self-centering due to the steel case at the nonemulative joint.

Results of Test Phase II

Damage Assessment

The apparent damage, assessed at 6.7% drift ratio for Specimens I and II, is shown in Fig. 14. No damage was observed in the cap beam for Specimens I and II. For both specimens, damage near the emulative joint included flexure-induced concrete cracking and shear cracking in the column region inserted into the steel brackets. No concrete spalling was observed due to flexure for either specimen owing to PVA fibers in UHPC. Specimen I had more severe rocking-induced damage at the east side than the west side due to the lack of symmetry in rocking and bending displacements, as discussed in section “Displacement Source.” Unlike Specimen I, Specimen II did not show any additional apparent damage at the nonemulative joint beyond Test Phase I.

Global Force-Displacement Response

Fig. 15 shows the lateral force versus lateral displacement responses of Test Phase II for both Specimens. Test Phase II started at 3.0% lateral drift ratio and ended when most of the initial

post-tension force was lost (Specimen I) or when lateral strength degraded (Specimen II).

Specimen I maintained its lateral strength without degradation throughout the test. The hysteresis loop shape was different in the positive and negative loading directions due to differences in rocking and bending contributions in the two loading directions, as discussed in section “Displacement Source.” For Specimen II, the lateral strength first dropped at 6.7% drift ratio in the negative direction due to concrete shear cracking within the steel brackets. Unlike Specimen I, pinching was evident in the beginning of Test Phase II for Specimen II due to its higher relative bending displacements.

Displacement Source

Lateral displacement was decomposed into displacements due to rocking (at the nonemulative joint) and due to bending (at the emulative joint), as shown in Fig. 16. For both specimens, the large area enclosed by the force-bending displacement hysteretic loops indicates that energy dissipation is achieved and is mostly due to bending.

Specimen I had much smaller rocking displacements when the pier was loaded toward east (negative loading) than it was loaded toward west, especially after 4.4% drift ratio. This can be explained

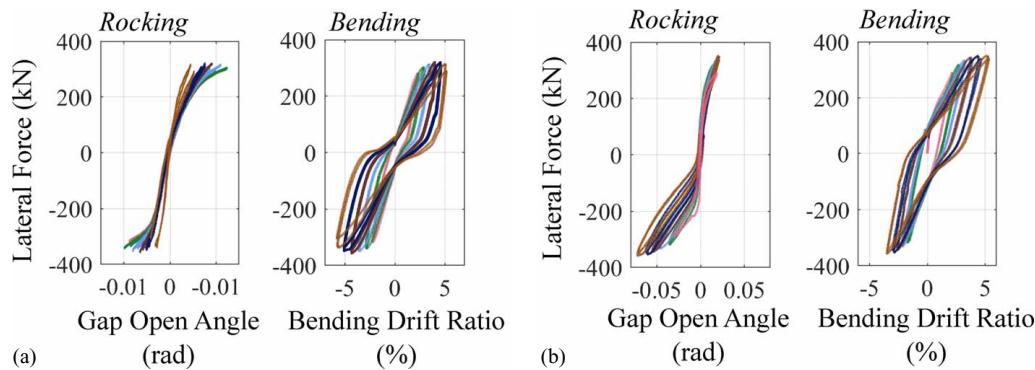


Fig. 16. Displacement decomposition of Test Phase II for (a) Specimen I; and (b) Specimen II.

by significant concrete spalling near the east side of the nonemulative joint and loss of post-tension force in the strands on the west side. Small energy dissipation observed through rocking displacements of Specimen I is due to yielding of the eccentrically located post-tension strands at 3.8% drift ratio. For Specimen II, all strands remained within their elastic limit throughout the test. Rocking response had negligible residual displacements as the top of the bending segment was protected from spalling with a steel case. Pinching of the hysteretic loops is likely a reflection of the prying action within the steel brackets.

Comparison of Seismic Performance Metrics

The behavior of the hybrid pier specimens is compared in terms of different metrics. Test Phases I and II were combined for these comparisons. For the figures presented in this section, each data point represents the average value of the two repeated cycles at each displacement amplitude.

Bending Contribution Ratio

The bending contribution ratios of the hybrid pier specimens are compared at varying displacement amplitudes in Fig. 17. Table 3 summarizes the damage condition at critical drift ratios. During Test Phase I, Specimen I had a bending contribution ratio similar to Specimen II in Test Phase I before the formation of the vertical crack near the nonemulative joint due to rocking. This rocking-induced damage resulted in the bending contribution ratio to decrease from 73% at the drift ratio of 2.3% to 64% at the drift ratio of 3.0%. During Test Phase II, Specimen I had a smaller bending contribution than Specimen II because of the higher post-tension loss and concrete spalling at the nonemulative joint in Specimen I. Both post-tension loss and concrete spalling are expected to reduce the rocking stiffness. For Specimen I, the bending contribution ratio was 61% averaged over the drift ratios in the range of 3.0%–6.8%. In general, protection of the nonemulative joint from damage enabled Specimen II to develop a stable balance between bending and rocking displacements. At smaller drift ratios (<0.5%), the hybrid system had more than 40% of its total displacement from rocking to facilitate self-centering. At larger drift ratios (>4.5%), bending contributed to 80% of the total displacement for energy dissipation.

Backbone Curve

The backbone curves of lateral force amplitude versus total displacement and versus bending drift ratio were compared for all

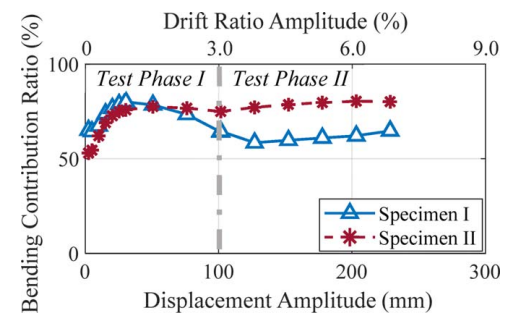


Fig. 17. Comparison of bending contribution ratios at varying displacement amplitudes.

Table 3. Damage progression

Test specimen	Test Phase I	Test Phase II
Specimen I	Rocking-induced damage: cracking initiated at 2.3% drift ratio and propagated until 3.0% drift ratio Flexure-induced damage: none	Rocking-induced damage: gradually increased from drift ratio of 3.0%–6.7% Flexure-induced damage: limited to cracking
Specimen II	Rocking-induced damage: limited to hairline cracking up to 3% drift ratio Flexure-induced damage: none	Rocking-induced damage: none between drift ratios of 3.0% and 6.7% Flexure-induced damage: limited to cracking

specimens, as shown in Figs. 18(a and b), respectively. For each cycle, the force amplitude was calculated as the average of the absolute value of the force at the peak positive and negative displacements. Specimens I and II had similar lateral strengths at varying bending drift ratios. The slightly larger lateral strength of Specimen I compared to that of Specimen II was due to the higher post-tension force in Specimen I caused by larger rocking displacements. This implies that the higher-confinement steel grade in Specimen II had a negligible influence on the flexural strength of UHPC. The confinement volumetric ratios of the UHPC bending segments in Specimens I and II were 54% and 109% of the minimum requirement of ACI 318-19 (ACI 2019), respectively. They correspond to 82% and 41% of the minimum requirement of AASHTO (2017). Neither specimen exhibited strength degradation until 4.0% bending drift ratio. For comparison, the bending drift ratio at which strength degradation started was 2.6% for a normal concrete hybrid pier due to concrete crushing within the socket

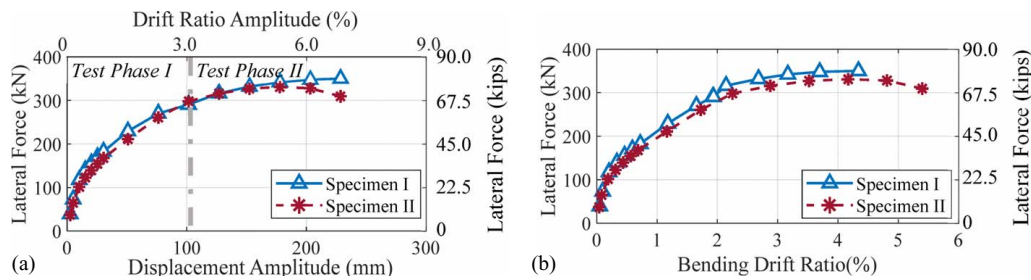


Fig. 18. Comparison of the backbone curves of force versus: (a) total displacement; and (b) bending drift ratio.

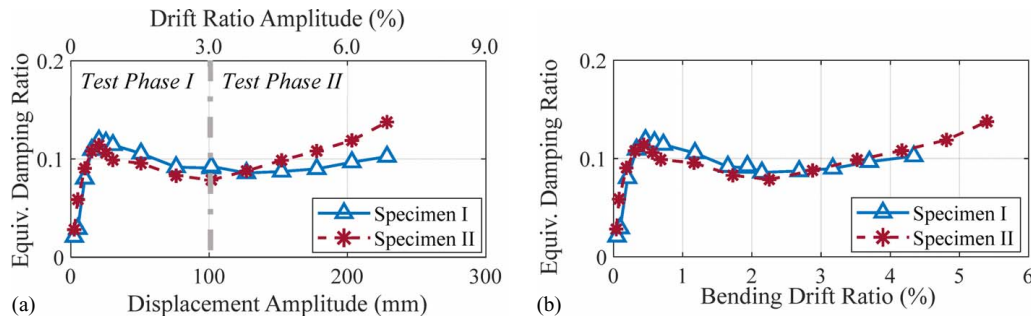


Fig. 19. Comparison of equivalent viscous damping ratios at varying: (a) displacement amplitudes; and (b) bending drift ratios.

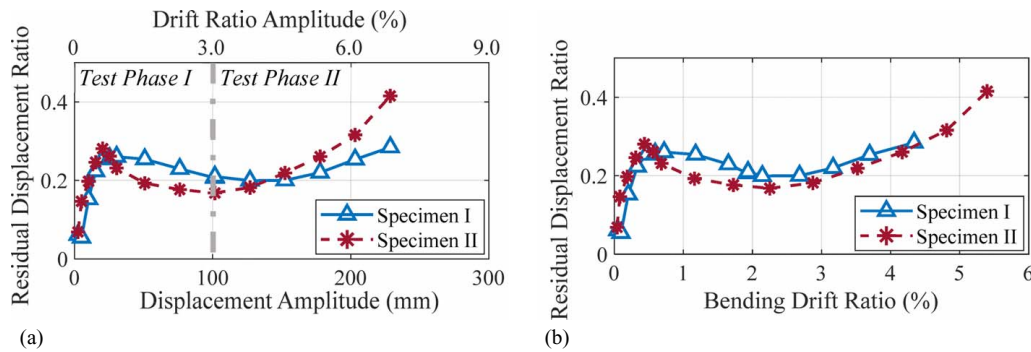


Fig. 20. Comparison of residual displacement ratios at varying: (a) displacement amplitudes; and (b) bending drift ratios.

region (Yang 2019). It was demonstrated that UHPC has the potential for maintaining strength by avoiding concrete crushing within the socket.

Energy Dissipation

Energy dissipation is defined as the area enclosed by the force–displacement hysteretic loops. Fig. 19(a) plots the equivalent viscous damping ratio versus displacement amplitudes for both specimens until their ultimate displacement. Fig. 19(b) shows the same with respect to the bending displacement ratio, as bending strongly influences energy dissipation. The equivalent viscous damping ratio was calculated according to Chopra (2017) for each loading cycle. In Test Phase I, the two specimens had similar equivalent damping ratios. In Test Phase II, Specimen II had higher energy dissipation than Specimen I due to larger bending displacements at the same displacement amplitude, as shown in Fig. 16. The similarities in the equivalent damping ratio between Specimens I and II are shown in Fig. 19(b). In general, energy dissipation was mainly provided by bending due to plastic hinging near the emulative joint (longitudinal reinforcement bar yielding, concrete cracking, and

crushing). Rocking contribution to energy dissipation was smaller and through contact damping, concrete cracking, and crushing at nonemulative joint and, for Specimen I, the yielding of post-tension strands. This indicates that energy dissipation highly depended on the bending contribution to displacement and the confinement steel grade had a negligible impact on energy dissipation.

Self-Centering

Self-centering ability was quantified using a residual displacement ratio, which was calculated as the ratio of the total residual displacement at the end of each cycle to the total peak displacement at that cycle. Lower values of the residual displacement ratio indicate better self-centering. Fig. 20(a) plots the residual displacement ratio versus displacement amplitude for both specimens. Fig. 20(b) shows the residual displacement ratio versus bending drift ratio as the displacement source has a strong influence on self-centering. In Test Phase I, Specimen I exhibited slightly larger residual displacements compared to Specimen II, despite having a smaller bending contribution to displacements. This was likely due to damage near the nonemulative joint. However, at larger displacements,

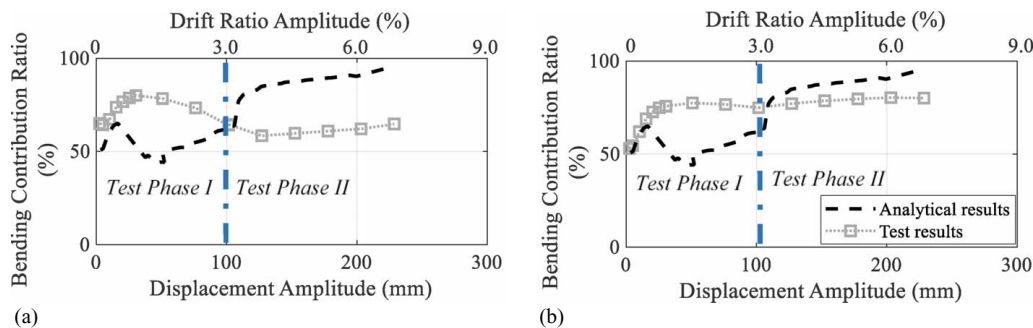


Fig. 21. Comparison of the bending contribution ratio from analytical models and tests for (a) Specimen I; and (b) Specimen II.

self-centering was highly dependent on the displacement source, as shown in Fig. 19(b). The grade of confinement steel had a negligible impact on self-centering.

Evaluation of the Analytical Models with Experimental Results

This section evaluates the applicability of the analytical model that have been used to design hybrid piers and to select UHPC mix for the bending segment. The analytical model is presented in section “Concept and Design Methods of Hybrid Precast Pier.” The evaluation was performed by comparing the bending contribution ratios obtained from the analytical model and tests for Specimens I and II, as shown in Fig. 21. For both Specimens I and II, the analytical model underestimated the bending contribution ratio in Test Phase I. This is mainly because the analytical model assumes a perfectly fixed emulative joint and neglected the slip of column from the foundation. During Test Phase II, the bending contribution ratio calculated by the analytical model was much higher than the one obtained from testing for Specimen I. This is mainly because the analysis did not include the damage to the rocking joint during Test Phase I. Specimen II had a steel case on the rocking joint during both Test Phases I and II, the damage at the nonemulative joint was effectively lowered. The inability of the analytical model to capture damage at the nonemulative joint due to rocking had less impact on the accuracy of the analytical model for Specimen II. Therefore, the analytical model predicted the bending contribution ratio reasonably well for Test Phase II.

Summary and Conclusions

This paper investigates using UHPC in hybrid precast concrete piers under cyclic loading to minimize spalling and to better distribute cracking. The hybrid pier is composed of a bending segment and rocking segments. A UHPC mix is selected for the bending segment through material testing and analyses of pier behavior with varying mixes. Large-scale testing of two pier specimens with the selected UHPC mix is performed. The specimens have different confinement reinforcement grades (confinement volumetric ratios). The major conclusions regarding the analytical investigation are as follows:

- The design philosophy of the hybrid pier is to allow both bending and rocking to contribute to the lateral displacement. Reinforcement of the bending segment, post-tension at the nonemulative joint, and concrete strength are selected for a desired bending to rocking displacement ratio. The bending contribution ratio (the ratio of bending drift to total drift), calculated

by the analytical model, is used to evaluate the balance between bending and rocking for hybrid piers. This study adopts the average bending contribution ratio of 50% (comparable bending and rocking responses) for selecting an optimum UHPC mix for the bending segment.

- The analytical model is applied to hybrid concrete piers with varying UHPC mixes. Analysis results show that the bending contribution ratio (the ratio of bending drift to total drift) decreases with an increase in tensile toughness of UHPC used in the bending segment. UHPC mix with AN1000 mix design and 2% PVA fiber by volume is selected because it maintains the average bending contribution ratio at approximately 50% and has the greatest compressive toughness among all UHPC mixes considered.

The major conclusions regarding the experimental investigations are as follows:

- Test results show that UHPC hybrid piers with an initial post-tension force of 13% of the axial compression capacity calculated using the compressive strength of NC, with a height ratio of 54%, and with the longitudinal reinforcement ratios of the bending and rocking segments of 1.3% and 1.8%, respectively, can simultaneously undergo rocking and bending displacements. Rocking response correlates with self-centering, and bending correlates with energy dissipation. Bending displacements of the tested specimens vary between 53.0% and 82.4% of the total displacement.
- Controlling rocking-induced damage is essential to maintain the balance of bending and rocking for hybrid piers: When the non-emulative joint is not externally confined by a steel case, a vertical crack forms at the top of the bending segment right below the nonemulative joint at a drift ratio of 2.3% due to the lateral dilation caused by rocking-induced concentrated compression. This weakens the rocking response and increases the rocking displacements. The bending contribution decreases from 73% at a drift ratio of 2.3% to 64% at a drift ratio of 3.0%.
- The steel case is demonstrated to serve as an effective means for mitigating rocking-induced damage and develop a stable balance between bending and rocking displacements: When the rocking-induced damage is alleviated by the steel case confining the top of the bending segment, more than 40% of the total displacement is from rocking at smaller drift ratios (<0.5%). At larger drift ratios (4.5%), approximately 80% of the displacement is due to bending, enabling energy dissipation.
- Energy dissipation and self-centering have a positive and negative correlation with the bending contribution to displacements and are minimally impacted by the confinement steel grade in the bending segment.
- Replacing normal-strength steel with high-strength steel confinement does not have any adverse or beneficial effects on

the flexural behavior of UHPC. Both UHPC bending segments, with the confinement volumetric ratios of 53% and 106% of the minimum requirement of ACI 318-19 (ACI 2019) and with the confinement volumetric ratios of 41% and 82% of the minimum requirement of AASHTO (2017), reach at least 4.0% bending drift ratios without strength degradation, indicating that UHPC may not require the additional confinement required by ACI 318-19 (ACI 2019) and AASHTO (2017). It should be noted that UHPC columns tested have low axial loads (13% including post-tensioning) and low longitudinal reinforcement ratios (1.3%). The effects of confinement on UHPC columns with higher axial load and reinforcement ratios warrant further investigation.

Data Availability Statement

All data, models, or code that support the findings of this study are available from the corresponding author upon reasonable request.

Acknowledgments

This research was supported by the Institute of Bridge Engineering, and the Department of Civil, Structural and Environmental Engineering at University at Buffalo, the State University of New York. Contributions of LafargeHolcim and MMFX for donating materials are acknowledged. The results do not necessarily reflect the views of the funding agencies and the parties acknowledged.

References

- AASHTO. 2017. *AASHTO LRFD bridge design specifications*. 8th ed. Washington, DC: AASHTO.
- ACI (American Concrete Institute). 2019. *Building code requirement for reinforced concrete*. ACI 318-19. Farmington Hills, MI: ACI.
- Al-Jelawy, H. M., K. R. Mackie, and Z. B. Haber. 2018. "Shifted plastic hinging for grouted sleeve column connections." *ACI Struct. J.* 115 (4): 1101–1114.
- Ameli, M. J., and C. P. Pantelides. 2017. "Seismic analysis of precast concrete bridge columns connected with grouted splice sleeve connectors." *J. Struct. Eng.* 143 (2): 04016176. [https://doi.org/10.1061/\(ASCE\)ST.1943-541X.0001678](https://doi.org/10.1061/(ASCE)ST.1943-541X.0001678).
- ASTM. 2016. *Standard test method for compressive strength of hydraulic cement mortars*. ASTM C109/C109M. West Conshohocken, PA: ASTM.
- ASTM. 2017. *Standard practice for fabricating and testing specimens of ultra-high performance concrete*. ASTM C1856/C1856M. West Conshohocken, PA: ASTM.
- ASTM. 2019a. *Standard specification for deformed and plain, low-carbon, chromium, steel bars for concrete reinforcement*. ASTM A1035M. West Conshohocken, PA: ASTM.
- ASTM. 2019b. *Standard test method for flexural performance of fiber-reinforced concrete (using beam with third-point loading)*. ASTM C1609/C1609M. West Conshohocken, PA: ASTM.
- ASTM. 2020. *Standard specification for deformed and plain carbon-steel bars for concrete reinforcement*. ASTM A615/A615M. West Conshohocken, PA: ASTM.
- Baby, F., and B. Graybeal. 2012. "A proposed flexural test method and associated inverse analysis for UHPFRC." *ACI Mater. J.* 109 (5): 545–555.
- Baby, F., B. Graybeal, P. Marchand, and F. Toutlemonde. 2013. "UHPFRC tensile behavior characterization: Inverse analysis of four-point bending test results." *Mater. Struct.* 46 (8): 1337–1354. <https://doi.org/10.1617/s11527-012-9977-0>.
- Basereh, S., P. Okumus, and S. Aaleti. 2020. "Reinforced-concrete shear walls retrofitted using weakening and self-centering: Numerical modeling." *J. Struct. Eng.* 146 (7): 04020122. [https://doi.org/10.1061/\(ASCE\)ST.1943-541X.0002669](https://doi.org/10.1061/(ASCE)ST.1943-541X.0002669).
- Billington, S. L., and J. K. Yoon. 2004. "Cyclic response of unbonded post-tensioned precast columns with ductile fiber-reinforced concrete." *J. Bridge Eng.* 9 (4): 353–363. [https://doi.org/10.1061/\(ASCE\)1084-0702\(2004\)9:4\(353\)](https://doi.org/10.1061/(ASCE)1084-0702(2004)9:4(353)).
- Cai, Z.-K., Z. Wang, and T. Y. Yang. 2019. "Cyclic load tests on precast segmental bridge columns with both steel and basalt FRP reinforcement." *J. Compos. Constr.* 23 (3): 04019014. [https://doi.org/10.1061/\(ASCE\)CC.1943-5614.0000944](https://doi.org/10.1061/(ASCE)CC.1943-5614.0000944).
- Chopra, A. K. 2007. *Dynamics of structures: Theory and applications to earthquake engineering*. New Delhi, India: Prentice-Hall.
- Fang, C., D. Liang, Y. Zheng, M. C. H. Yam, and R. Sun. 2020. "Rocking bridge piers equipped with shape memory alloy (SMA) washer springs." *Eng. Struct.* 214: 110651. <https://doi.org/10.1016/j.engstruct.2020.110651>.
- FHWA (Federal Highway Administration). 2018. *EDC-2: Accelerated bridge construction (ABC)*. Washington, DC: FHWA.
- Graybeal, B. 2006. *Material property characterization of ultra-high performance concrete*. Technical Rep. No. FHWA-HRT-06-103. McLean, VA: FHWA.
- Guo, T., Z. Cao, Z. Xu, and S. Lu. 2016. "Cyclic load tests on self-centering concrete pier with external dissipators and enhanced durability." *J. Struct. Eng.* 142 (1): 04015088. [https://doi.org/10.1061/\(ASCE\)ST.1943-541X.0001357](https://doi.org/10.1061/(ASCE)ST.1943-541X.0001357).
- Haber, Z. B., K. R. Mackie, and H. M. Al-Jelawy. 2017. "Testing and analysis of precast columns with grouted sleeve connections and shifted plastic hinging." *J. Bridge Eng.* 22 (10): 04017078. [https://doi.org/10.1061/\(ASCE\)BE.1943-5592.0001105](https://doi.org/10.1061/(ASCE)BE.1943-5592.0001105).
- Haber, Z. B., M. S. Saiidi, and D. H. Sanders. 2014. "Seismic performance of precast columns with mechanically spliced column-footing connections." *ACI Struct. J.* 111 (3): 639–650. <https://doi.org/10.14359/51686624>.
- Haraldsson, O. S., T. M. Janes, M. O. Eberhard, and J. F. Stanton. 2013. "Seismic resistance of socket connection between footing and precast column." *J. Bridge Eng.* 18 (9): 910–919. [https://doi.org/10.1061/\(ASCE\)BE.1943-5592.0000413](https://doi.org/10.1061/(ASCE)BE.1943-5592.0000413).
- Jia, J., K. Zhang, M. S. Saiidi, Y. Guo, S. Wu, K. Bi, and X. Du. 2020. "Seismic evaluation of precast bridge columns with built-in elastomeric pads." *Soil Dyn. Earthquake Eng.* 128: 105868. <https://doi.org/10.1016/j.soildyn.2019.105868>.
- LafargeHolcim. 2009. "Ductal® JS1000." Accessed January 20, 2018. http://www.ductal.com/JS1000_2009.pdf.
- Liu, R. 2018. "Multi-performance seismic design of low damage bridge piers." Ph.D. thesis, Civil Engineering, Univ. of Canterbury.
- Marshall, C., J. Cantrell, M. Mashal, and A. Ebrahimpour. 2020. "A precast pier system for ABC in seismic regions." In *SEI Structures Congress*, edited by J. G. Soules, 183–192. Reston, VA: ASCE.
- Mashal, M., and A. Palermo. 2019a. "Low-damage seismic design for accelerated bridge construction." *J. Bridge Eng.* 24 (7): 04019066. [https://doi.org/10.1061/\(ASCE\)BE.1943-5592.0001406](https://doi.org/10.1061/(ASCE)BE.1943-5592.0001406).
- Mashal, M., and A. Palermo. 2019b. "Emulative seismic resistant technology for accelerated bridge construction." *Soil Dyn. Earthquake Eng.* 124: 197–211. <https://doi.org/10.1016/j.soildyn.2018.12.016>.
- Mashal, M., S. White, and A. Palermo. 2016. "Quasi-static cyclic testing of emulative cast-in-place connections for accelerated bridge construction in seismic regions." *Bull. N. Z. Soc. Earthquake Eng.* 49 (3): 267–282. <https://doi.org/10.5459/bnzsee.49.3.267-282>.
- Megally, S. H., M. Garg, F. Seible, and R. K. Dowell. 2002. *Seismic performance of precast segmental bridge superstructures*. Rep. No. SSRP-2001/24. San Diego: Dept. of Structural Engineering, Univ. of California.
- Mohebbi, A., M. S. Saiidi, and A. M. Itani. 2018a. "Shake table studies and analysis of a precast two-column bent with advanced materials and pocket connections." *J. Bridge Eng.* 23 (7): 04018046. [https://doi.org/10.1061/\(ASCE\)BE.1943-5592.0001247](https://doi.org/10.1061/(ASCE)BE.1943-5592.0001247).
- Mohebbi, A., M. S. Saiidi, and A. M. Itani. 2018b. "Shake table studies and analysis of a PT-UHPC bridge column with pocket connection."

- J. Struct. Eng.* 144 (4): 04018021. [https://doi.org/10.1061/\(ASCE\)ST.1943-541X.0001997](https://doi.org/10.1061/(ASCE)ST.1943-541X.0001997).
- Nikoukalam, M. T., and P. Sideris. 2017. "Resilient bridge rocking columns with polyurethane damage-resistant end segments and replaceable energy-dissipating links." *J. Bridge Eng.* 22 (10): 04017064. [https://doi.org/10.1061/\(ASCE\)BE.1943-5592.0001069](https://doi.org/10.1061/(ASCE)BE.1943-5592.0001069).
- Ou, Y.-C., P.-H. Wang, M.-S. Tsai, K.-C. Chang, and G. C. Lee. 2010. "Large-scale experimental study of precast segmental unbonded post-tensioned concrete bridge columns for seismic regions." *J. Struct. Eng.* 136 (3): 255–264. [https://doi.org/10.1061/\(ASCE\)ST.1943-541X.0000110](https://doi.org/10.1061/(ASCE)ST.1943-541X.0000110).
- Sideris, P., A. J. Aref, and A. Filiatrault. 2014. "Quasi-static cyclic testing of a large-scale hybrid sliding-rocking segmental column with slip-dominant joints." *J. Bridge Eng.* 19 (10): 04014036. [https://doi.org/10.1061/\(ASCE\)BE.1943-5592.0000605](https://doi.org/10.1061/(ASCE)BE.1943-5592.0000605).
- Steuck, K. P., M. O. Eberhard, and J. F. Stanton. 2009. "Anchorage of large-diameter reinforcing bars in ducts." *ACI Struct. J.* 106 (4): 506–513.
- Tazarv, M., and M. Saiid Saiidi. 2016. "Low-damage precast columns for accelerated bridge construction in high seismic zones." *J. Bridge Eng.* 21 (3): 04015056. [https://doi.org/10.1061/\(ASCE\)BE.1943-5592.0000806](https://doi.org/10.1061/(ASCE)BE.1943-5592.0000806).
- Tong, T., W. Zhuo, X. Jiang, H. Lei, and Z. Liu. 2019. "Research on seismic resilience of prestressed precast segmental bridge piers reinforced with high-strength bars through experimental testing and numerical modelling." *Eng. Struct.* 197: 109335. <https://doi.org/10.1016/j.engstruct.2019.109335>.
- Wang, Z., J. Wang, J. Liu, F. Han, and J. Zhang. 2019. "Large-scale quasi-static testing of precast bridge column with pocket connections using noncontact lap-spliced bars and UHPC grout." *Bull. Earthquake Eng.* 17 (9): 5021–5044. <https://doi.org/10.1007/s10518-019-00649-6>.
- Wang, Z., J. Wang, Y. Tang, T. Liu, Y. Gao, and J. Zhang. 2018. "Seismic behavior of precast segmental UHPC bridge columns with replaceable external cover plates and internal dissipaters." *Eng. Struct.* 177: 540–555. <https://doi.org/10.1016/j.engstruct.2018.10.012>.
- Xu, L., J. Pan, and J. Cai. 2019. "Seismic performance of precast RC and RC/ECC composite columns with grouted sleeve connections." *Eng. Struct.* 188: 104–110. <https://doi.org/10.1016/j.engstruct.2019.03.022>.
- Yang, C. 2019. "Reducing earthquake-induced damage to precast concrete bridge piers." Ph.D. thesis, Dept. of Civil, Structural and Environmental Engineering, State Univ. of New York at Buffalo.
- Yang, C., and P. Okumus. 2017a. "Mechanical behavior and prestress loss of unbonded posttension strands in self-centering structures." *J. Mater. Civ. Eng.* 29 (12): 04017245. [https://doi.org/10.1061/\(ASCE\)MT.1943-5533.0002097](https://doi.org/10.1061/(ASCE)MT.1943-5533.0002097).
- Yang, C., and P. Okumus. 2017b. "Ultrahigh-performance concrete for posttensioned precast bridge piers for seismic resilience." *J. Struct. Eng.* 143 (12): 04017161. [https://doi.org/10.1061/\(ASCE\)ST.1943-541X.0001906](https://doi.org/10.1061/(ASCE)ST.1943-541X.0001906).
- Yang, C., P. Okumus, and R. Ren. 2019. "A hysteretic model for self-centering precast concrete piers with varying shear-slip between segments." *Eng. Struct.* 188: 350–361. <https://doi.org/10.1016/j.engstruct.2019.01.053>.